Quantum chemical modeling of tri-Mn-substituted W-based Keggin polyoxoanions

Alena Kremleva[a], Pablo A. Aparicio[b], Alexander Genest[c], Notker Rösch[a,b,c,*]

[a] Department Chemie, Technische Universität München, 85747 Garching, Germany

[b] TUM CREATE Limited, 1 CREATE Way, #10-02 Create Tower, Singapore 138602, Singapore

[c] Institute of High Performance Computing, Agency for Science, Technology and Research, 1 Fusionopolis Way, #16-16 Connexis, Singapore 138632, Singapore

ARTICLE INFO

To Professor Maria-Elisabeth Michel-Beyerle, TUM CREATE Singapore, who, over many years, generously shared her deep insight into a broad range of prob-lems in physical chemistry and provided outstanding leadership in forming highly successful, long-term research alliances for solving such problems.

Keywords:
Polyoxometalates
Keggin ion
Redox potentials
DFT modeling
Electrolyte environment

ABSTRACT

Using Density Functional Theory (DFT) calculations, we studied the electrochemistry of polyoxome-talates (POMs), specifically the redox properties of Mn in tri-Mn-substituted W-based Keggin ions. For direct comparison with recent cyclic voltammetry results [J. Friedl et al. Electrochim. Acta, 141 (2014) 357], we estimated the reversible half-wave potentials of proton- and cation-coupled electron transfer for Mn(IV/III) and Mn(III/II), respectively. The calculated reversible potentials agree well with experiment, reproducing the trend with pH for Mn(IV/III). For adequate DFT energies, it is crucial to apply a reliable description of the electrolyte environment of the POM, accounting also for their rather high charges, up to 7 e. To this end, we included the Li^+ counterions, required for charge neutralization, directly in the quantum chemical models which were embedded in a polarizable continuum. We explored various arrangements of the Li^+ ions around the POMs and their effect on both structural parameters and electrochemical properties of the POMs. Hybrid functionals (TPSSh, B3LYP, PBE0) overestimate the experimental reduction potentials: the larger the exact-exchange contribution, the larger the resulting reduction potential. The best agreement with experiment is achieved with the PBE approach, likely due to fortuitous error cancellation. The results of the present work indicate that a more sophisticated (atomistic) representation of the electrolyte environment will be beneficial for predicting redox potentials in better agreement with experiment.

1. Introduction

Polyoxometalates (POMs) are a class of nano-sized compounds formed by linking early transition metal polyhedra via oxygen centers located at their vertices [1–4]. POMs exist in a variety of shapes, sizes, and compositions [2,5,6]. They are stable over a wide range of pH values and temperatures and they are able to undergo reversible multi-electron redox processes [7–9]. Therefore, POMs can be employed in electrocatalysis, including hydrogen evolution reactions [10]. POMs can be regarded as a molecular “electron sponge” due to many-electron redox processes; they have been proposed as a cathode material for high-performance rechargeable batteries, so-called molecular cluster batteries [8,9].

Recently, the use of POMs has also been suggested for large-scale energy storage, in particular in redox flow batteries (RFB) [11]. In this context, attention focused in particular on so-called Keggin ions, i.e., structures of the type $[XM_{12}O_{40}]^n$ [3,4]. The highly symmetric Keggin ion with M = W and X = P was the first such structure to be clarified by X-ray diffraction [3]. Formal replacement of some centers M by another transition metal M^0 generates Keggin-type POMs where redox potentials due to the two types of metals are separated by up to a few Volts [12–14]. As an example, we mention V-exchanged W-based Keggin ions [12], a system which was shown to yield an aqueous 0.8 V battery that could be cycled 100 times, achieving a Coulombic efficiency above 95% [12]. Although the current densities of this prototype were measured at least one order lower than those of common RFBs [15], POMs based systems may offer a new approach to RFBs.

Inspired by this new concept, another substituted POM, namely a tri-Mn-substituted W-based Keggin ion (X = Si) was recently introduced and examined electrochemically [13,16]. The initial oxidation state of this POM has been shown to affect the Mn electrochemistry, whereas the nature of the counterions was found not to influence the resulting electrochemistry [13].

* Corresponding author at: Department Chemie, Technische Universität München, 85747 Garching, Germany.

E-mail address: roesch@mytum.de (N. Rösch).

Computational chemistry offers an approach complimentary to experiment, for characterizing the (electrochemical) properties of POMs [17–24]; see also some reviews [25–27] and the references therein. Thus far, structural parameters, electronic properties, and the magnetism of POMs have been computationally examined [17,18,21,25]. Solvation effects on the properties of POMs were also explored in this way [28–30], including those of a surrounding electrolyte [29,30].

To the best of our knowledge, there is only one computational study on the redox properties of singly-substituted Keggin ions
[31]. In that work, no explicit counterions were included in the model, and solvation of the highly charged POMs was modeled by the continuum COSMO model [32]. Such simplifications led to significant uncertainties in the absolute reduction potentials. However, shifts of the reduction potentials, relative to the unsubstituted Keggin ion, successfully reproduced the correspond-ing experimental trends [31]. A similar approach was used to study the redox properties of Dawson-type POMs [33,34].

The present computational study is motivated by experimental investigations on the Mn-redox behavior of tri-Mn-substituted W-based Keggin systems [13]. By means of density functional theory (DFT) calculations, we present a model study of the reversible half-wave redox potentials for two types of reactions, namely proton-coupled electron transfer in the case of Mn(IV/III) and cation-coupled electron transfer in the case of Mn(III/II). For achieving an adequate DFT energetics, we modeled the structure of these systems for various oxidation states of the Mn centers, and we explored structural aspects of the surrounding electrolyte as well as Mn-related standard reduction potentials and their relation to the experimentally measured reversible redox potentials. We also aimed at identifying a consistent DFT approach for modeling absolute redox potentials by exploring several exchange-correla-tion functionals.

2. Models and Methods

2.1. Models of metal-substituted Keggin ions

The original Keggin ion has the general formula of $[XM_{12}O_{40}]^n$, with a heteroatom X at the center of a spherical arrangement of metal atoms M; its structure is referred to as a-ion [3]. Other isomers (b-, g-, etc.) are derived from this structure by successive rotations of W_3O_{13} units by 60 [35]. The present study addresses an a-Keggin ion with X = Si, M = W (fully oxidized), where three neighboring M centers directly above the triangular face of the central SiO_4 tetrahedron are substituted by M^0 = Mn, the latter in oxidation states (IV), (III), or (II) (Fig. 1). Such a substitution pattern is referred to as A-type structure [36]. Fig. 1a shows a sketch of the calculated (optimized) structure of the fully oxidized system $[Mn(IV)_3(OH)_3(OH)_3(A\text{-}a\text{-}SiW_9O_{34})]^4$ [16]. Each Mn center exhibits one terminal OH ligand; among each other, the Mn centers are connected by bridging OH groups. Each Mn center is connected to a W center via a binding O_W center, and to Si via O_{Si} centers (Fig. 1a).

In an aqueous solution and in the crystal structure, the relatively high charge of the POM is neutralized by counterions. Following the experiment [13], we used Li^+ as counterions. The reduction of Mn centers to oxidation state (III) is coupled with a proton transfer as demonstrated experimentally by the pH dependence of the redox potential for Mn(IV/III) [13]:

$$Li_4[Mn(IV)_3(OH)_3(OH)_3(A\text{-}a\text{-}SiW_9O_{34})] + 3e + 3H^+ \; ! \; Li_4[Mn(III)_3(OH)_3(OH_2)_3(A\text{-}a\text{-}SiW_9O_{34})] \quad (1)$$

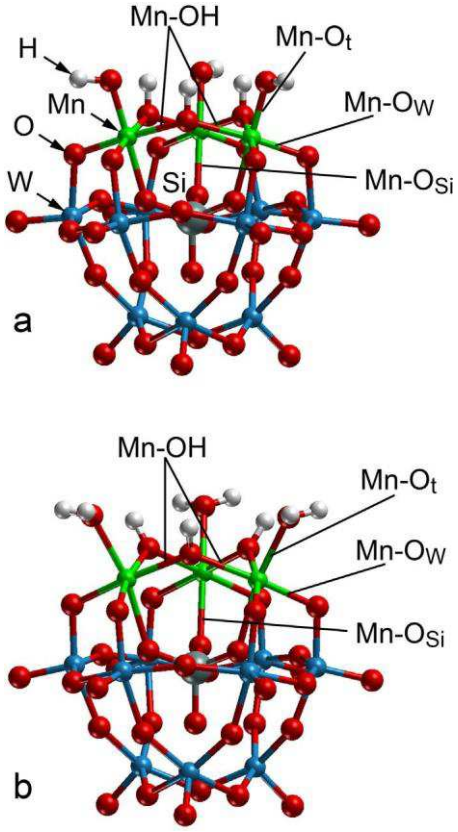

Fig. 1. Schematic representations of tri-Mn-substituted Keggin ions with important Mn-O bonds labeled: (a) $[Mn(IV)_3(OH)_3]^4$, (b) $[Mn(III)_3(H_2O)_3]^4$. Atom labels shown for structure a.

Therefore, after reducing all Mn centers to oxidation state (III), one obtains $[Mn(III)_3(OH)_3(OH_2)_3(A\text{-}\alpha\text{-}SiW_9O_{34})]^4$, Fig. 1b. The most obvious difference to the POM with Mn(IV) centers are the terminal ligands, OH_2 instead of OH, of the Mn centers, Fig. 1. The systems with the three Mn centers further reduced corresponds to $[Mn(II)_3(OH)_3(OH_2)_3(A\text{-}\alpha\text{-}SiW_9O_{34})]^7$:

$$Li_4[Mn(III)_3(OH)_3(OH_2)_3(A\text{-}\alpha\text{-}SiW_9O_{34})] + 3e + 3Li^+ \rightarrow Li_7[Mn(II)_3(OH)_3(OH_2)_3(A\text{-}\alpha\text{-}SiW_9O_{34})] \quad (2)$$

This equation reflects the fact that almost constant values of the Mn(III/II) redox potential were measured over a pH range [13]. These findings suggested a cation-coupled electron transfer mechanism for the latter reduction process.

Eqs. (1) and (2) are written for a single transfer step of 3 e , but in experiment electron transfer occurs in a one-by-one fashion [13]. At least for the reduction Mn(IV/III), these 1 e transfer steps have been discriminated; see Fig. 3b in Ref. [13]. In the present study, we considered simplified models representing the simulta-neous transfer of 3 e ; see Eqs. (1) and (2). We also tested non-symmetrical structures with only one or two Mn centers reduced. A charge analysis showed that the corresponding charges were well localized for all exchange-correlation functionals studied, including the generalized gradient approximation (GGA) PBE [37] where sometimes self-interaction artifacts are observed [38]. Then the redox potentials calculated for the transfer of a single e (Section 3.3) have to be compared to suitable averages of experimental values. The corresponding experimental redox potentials, however, are rarely distinguished. For the system under study experiments revealed very close lying peaks, differing by 0.2 V only [13]. Therefore, it seemed justified to employ simplified models, formally connected by the simultaneous transfer of 3 e . The fragment $(A\text{-}\alpha\text{-}SiW_9O_{34})$ comprises the W centers and the central SiO_4 tetrahedron. This moiety does not participate directly in the redox reaction processes under study, Eqs. (1) and (2). For improved readability, we therefore will not carry this fragment in the labels used in the following. In the same spirit, we will also drop from the simplified labels the bridging OH groups connecting neighboring Mn centers. Hence, in the following, we will refer to the systems with all Mn centers in the same oxidation state as $Li_4[Mn(IV)_3(OH)_3]$, $Li_4[Mn(III)_3(OH_2)_3]$, and $Li_7[Mn(II)_3(OH_2)_3]$.

2.2. Computational Method

We carried out first-principles DFT calculations with the software package TURBOMOLE 6.6 [39–41]. We employed the GGA functional PBE [37] as well as the hybrid approaches B3LYP [42,43], PBE0 [44], and TPSSh [45]. To accelerate the DFT calculations, we applied the resolution-of-identity (RI-J) approxi-mation for evaluating the Coulomb part of the electron-electron interaction together with a suitable auxiliary basis set [46]. We represented the Kohn-Sham orbitals using standard triple-zeta basis sets [47] together with effective core pseudopotentials for Mn [48] and W [49]. All systems studied are open-shell systems; therefore we used the unrestricted Kohn-Sham (UKS) formalism. In the geometry optimizations, the total energy was converged to 10^{-6} au. For the structure optimizations, the energy gradients on all atomic centers were required to be less than 10^{-3} au. All stationary structures of complexes in the gas phase were confirmed as local minima by a normal mode analysis.

The total Gibbs free energy G of a system was calculated as follows:

$$G = E_{el} + \Delta G_{solv} - RT \ln(q_{trans} q_{rot} q_{vib}) \quad (3)$$

Here, E_{el} is electronic energy of the system in the gas phase, ΔG_{solv} is the free energy of solvation; both quantities were evaluated for each of the functionals mentioned above. The thermochemistry was evaluated for room temperature, T = 298.15 K, and normal pressure, 1 atm. The term RT ln ($q_{trans}q_{rot}q_{vib}$) accounts for thermal corrections to the enthalpy and entropic terms (including zero-point energy). The latter correction term in Eq. (3) was evaluated for structures in the gas phase, optimized at the PBE level, using harmonic vibrational frequencies; the same values were also applied for correcting the energy quantities determined with the hybrid functionals.

The free energy of solvation ΔG_{solv} was estimated using the polarized continuum solvation model COSMO as implemented in TURBOMOLE [32]. The solute was embedded in a dielectric medium, water in the present study. The dielectric constant of water was set to 78.4. The molecular cavity in the dielectric medium was constructed from overlapping spheres with radii $R_i + R_{solv}$ for all atoms i. We used R_{solv} = 130 pm and the atomic radii R(Si) = 220 pm, R(W) = R(Mn) = 222 pm, R(O) = 172 pm, R(H) = 130 pm, and R(Li) = 157 pm. More details on the construction of the cavity can be found in Ref. [32]. To reduce the uncertainties associated with the polarized continuum description of solvation [50] (of small charged species), we used experimental values for the enthalpies of solvation of a proton, 1104.5 kJ mol^{-1}, and of a Li^+ ion, 519 kJ mol^{-1} [51,52], when deriving the corresponding free energies of solvation.

Model-related computational details describing how we calculated the redox potentials are given below in the correspond-ing sections.

3. Results and Discussion

An important aspect of modeling POMs and their redox potentials is the role of the counterions in the surrounding electrolyte, or, in other words, the screening effect of the electrostatic field due to the electrolyte. The (average) number of counterions in the immediate vicinity of the POM is estimated from the charge of the POM, i.e. the number of Li^+ counterions to render the nanooxidic cluster plus its immediate environment neutral. The interaction of various Keggin ions with their surrounding counterions in aqueous solution has been studied by means of molecular dynamics simulations using a force field [29]. These simulations showed that POMs and counterions may form configurations in analogy to contact ion pairs (inner-sphere interaction) as well as configurations in analogy to solvent-separated ion pairs (outer-sphere interaction). We decided to include the counterions into our quantum chemical model cluster, thus representing inner-sphere adsorbed Li^+ ions. For test purposes, we also calculated redox potentials for bare (and therefore highly charged) substituted Keggin ions and obtained a negative value for the reduction potential of the Mn(III/II) reduction. In view of this artifact, we decided to include explicitly an appropriate number of counterions in the models.

Section 3.1 describes various arrangements of the Li counter-ions chosen around the POM structure. In Section 3.2 we present the calculated results for the structural parameters of the neutral POMs and their dependence on the Li arrangements. In Section 3.3 we discuss how the Li cation arrangements affect the calculated standard redox potentials. Finally, in Section 3.4, we compare the calculated results for reversible redox potentials with experiment.

3.1. Distributing Li counterions on the surface of a Keggin ion

The models of tri-Mn-substituted POMs studied here exhibit 4 Li^+ counterions for the structures with Mn(IV) and Mn(III) centers and 7 Li^+ counterions for the structures with the fully reduced

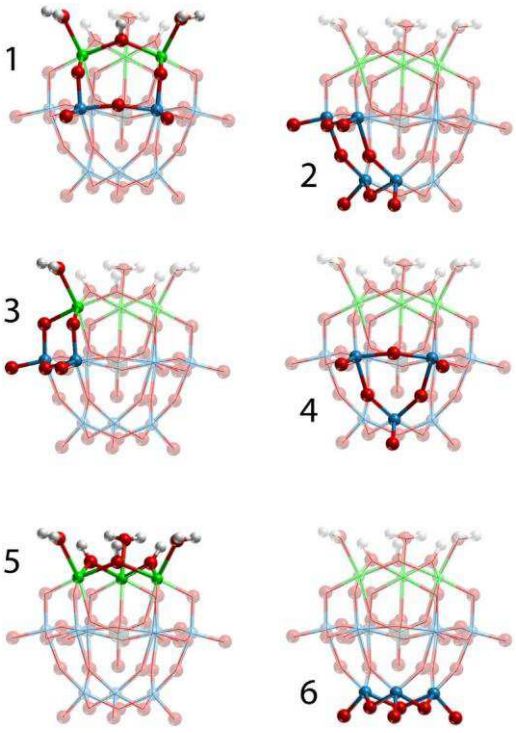

Fig. 2. Schematic representation of sites 1 to 6, for Li^+ inner-sphere adsorption on the tri-Mn-substituted Keggin ion $[Mn(III)_3(H_2O)_3]^4$ as example.

centers Mn(II). To explore the effect of how the Li cations are distributed around the POM structure within the present computational approach and to understand which sites on the surface of the tri-Mn-substituted POM anions under study may be occupied by Li ions, we first calculated the energies of a single Li^+ ion at six sites on the surface of this POM structure (Fig. 2). As discussed in Section 2, we focused on models where the three Mn centers were uniformly in one of the three oxidation states under study. On the surface of a tri-Mn-substituted Keggin ion, there are two 4-fold hollow sites (pockets), namely site 1 and site 2 (Fig. 2); these sites exhibit four nearby O centers of POM surface that are able to coordinate a Li cation. Sites 3 to 6 are 3-fold hollow sites, with three nearby O centers for Li coordination.

To quantify the site stability, we estimated binding energies E_b of a Li cation to POM as the reaction energy of the following formal transformation:

$$\text{Li-POM}^{(n\ 1)}\ (aq)\ !\ \text{POM}^{n}\ (aq) + \text{Li}^{+}(aq) \quad (4)$$

Table 1 collects the corresponding E_b values for $Li[Mn\ (IV)_3(OH)_3]^3$, $Li[Mn(III)_3(OH_2)_3]^3$, and $Li[Mn(II)_3(OH_2)_3]^6$. The cation Li^+ always binds stronger to a specific site of $[Mn\ (II)_3(OH_2)_3]^7$ than to the analogous sites of $[Mn(III)_3(OH_2)_3]^4$ and $[Mn(IV)_3(OH)_3]^4$, because of the Coulomb interaction. The total formal charge of the bare Keggin ion is 7 e of Mn(II) centers and 4 e in the case of Mn(III) and Mn(IV). For all sites except site 5, the binding strength increases when Mn is reduced. For example, Li binds with E_b = 0.90 eV to site 1 of $[Mn(IV)_3(OH)_3]^4$, with E_b = 1.06 eV to the analogous site of $[Mn(III)_3(OH_2)_3]^4$, and with E_b = 1.62 eV to $[Mn(II)_3(OH_2)_3]^7$. At site 5, Li^+ binds stronger to $[Mn\ (IV)_3(OH)_3]^4$, E_b = 1.03 eV, than to $[Mn(III)_3(OH_2)_3]^4$, E_b = 0.90 eV. In that case, the terminal OH ligands of $[Mn(IV)_3(OH)_3]^4$ coordinate to Li^+ ($Li\text{-}O_t$ = 282 pm) in addition to the bridging hydroxyls ($Li\text{-}OH_b$ = 202 pm) and thus render the binding of the counterion with the POM overall stronger. In contrast, $[Mn\ (III)_3(OH_2)_3]^4$ exhibits OH_2 terminal ligands and therefore is able to provide only weaker coordinative bonds to a Li cation at site 5 ($Li\text{-}O_t$ = 294 pm, $Li\text{-}OH_b$ = 202 pm). Note that these effects in part are a consequence of our model which does not offer any explicit solvation by water molecules. In a more realistic model, the terminal OH ligands would be shielded ("saturated") by nearby solvation water molecules. Therefore, we consider the unusual trend for site 5 as a model artifact.

Next, we compare the binding energies at different sites for a given structure with a uniform oxidation state of the Mn centers. For each oxidation state, sites 3, 4, and 6 are less favorable than the other sites (Table 1). For $[Mn(IV)_3(OH)_3]^4$ the most favorable Li position is site 5 with E_b = 1.03 eV (Table 1) which may reflect some aspects of the model, as just discussed. Sites 1 and 2 are rather close in energy, 0.90 and 0.81 eV, with site 1 being slightly favored. For $[Mn(III)_3(OH_2)_3]^4$, site 2 is the most favorable site for coordinating a single Li^+, E_b = 1.10 eV, site 1 is only 0.04 eV less favorable. Site 5 is 0.20 eV less favorable, compared to site 2 (Table 1). In conclusion, for both $[Mn(IV)_3(OH)_3]^4$ and $[Mn\ (III)_3(OH_2)_3]4$, we consider sites 1 and 2 as primary Li locations.

On the surface of the POM, there are three sites 1 and three sites 2, to be occupied by 4 Li cations, thus giving rise to several arrangements of Li counterions. We examined four of them, Fig. 3a–d. First, we assumed that all three sites 1 are occupied by Li cations, and the fourth Li occupies site 2 (Fig. 3a). We refer to this arrangement by the label 1_32_1 and we assume that the three structures of this type are essentially equivalent. A structurally different arrangement is 1_12_3, with three sites 2 and one site 1 occupied by Li^+ (Fig. 3b). In addition, we studied configurations

Table 1

Calculated binding energies[a] E_b (in eV) for a single Li cation probed on six sites of a tri-Mn-substituted Keggion ion with Mn in oxidation states (IV), (III), and (II).

Site[b]	1	2	3	4	5	6
Mn(IV)	0.90	0.81	0.62	0.53	1.03	0.24
Mn(III)	1.06	1.10	0.86	0.84	0.90	0.47
Mn(II)	1.62	1.59	1.16	1.26	1.64	0.90

[a] Results for the PBE exchange-correlation functional.
b For the site designations, see Fig. 2.

where two Li cations adsorb at sites 1 and two more at sites 2. There are two such isomers, with the Li cations positioned in symmetric or antisymmetric fashion (Fig. 3c, d), labeled $1_2 2_2$ sym and $1_2 2_2$ asym. We probed these four Li arrangements for both $Li_4[Mn(IV)_3(OH)_3]$ and $Li_4[Mn(III)_3(OH_2)_3]$.

On the surface of $[Mn(II)_3(OH_2)_3]^{7}$, sites 1, 2, and 5 exhibit rather similar binding energies E_b per Li cation, between 1.59 eV and 1.64 eV (Table 1). Therefore, one may assume all seven available sites of types 1, 2, and 5 to be occupied by 7 Li^+ counterions, required for a charge balance of $[Mn(II)_3(OH_2)_3]^{7}$. In this case we studied arrangement $1_3 2_3 5_1$ with 7 Li occupying sites 1, 2, and 5 (Fig. 3e). In addition, we optimized the structure where site 6 occupied instead of site 5, i.e., arrangement $1_3 2_3 6_1$ (Fig. 3f).

3.2. Structural parameters of the neutral oxide moiety

For each POM with a uniform oxidation state of the Mn centers, Table 2 presents results of PBE calculations for important

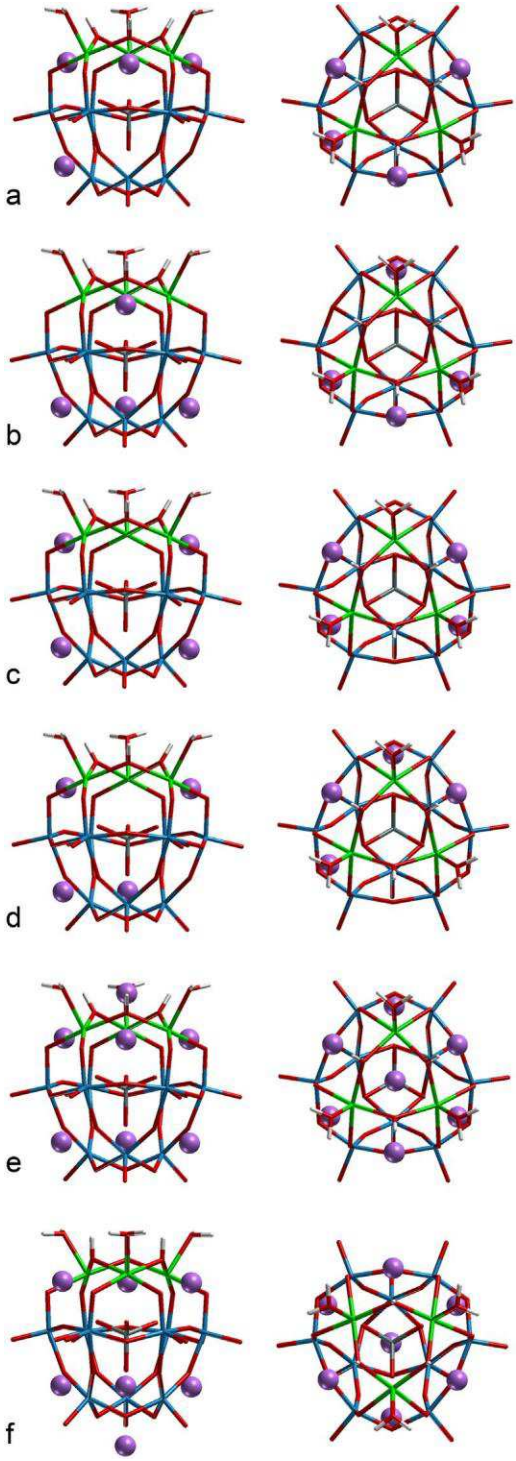

Fig. 3. Schematic representation of various Li arrangements for $Li_4[Mn(IV)_3(OH)_3]$ and $Li_4[Mn(III)_3(OH_2)_3]$ systems: (a) $1_3 2_1$, (b) $1_1 2_3$, (c) symmetric arrangement $1_2 2_2$ sym, (d) antisymmetric arrangement $1_2 2_2$ asym. Analogous sketches for $Li_7[Mn(II)_3(H_2O)_3]$ system: (e) $1_3 2_3 5_1$ and (f) $1_3 2_3 6_1$. Left column side view, right column top view. Li ions are shown as spheres, while the POM structure is represented by lines. For the atom labels, see Fig. 1.

Table 2
Structure parameters[a] (in pm) of $Li_4[Mn(IV)_3(OH)_3]$, $Li_4[Mn(III)_3(OH_2)_3]$, and $Li_7[Mn(II)_3(OH_2)_3]$ for various Li arrangements, calculated at the PBE level of theory. Relative total energies E_{rel} (in eV) are also given. For the site designations, see Figs. 2 and 3.

	Ion configuration	Mn-O_t	Mn-OH	Mn-O_W	Mn-O_{Si}	E_{rel}
$Li_4[Mn(IV)_3(OH)_3]$	$1_3 2_1$	180(0)	202(1)	186(1)	204(0)	0.00
	$1_1 2_3$	180(0)	198(2)	188(2)	205(1)	0.23
	$1_2 2_2$, sym	180(0)	201(2)	187(2)	205(1)	0.15
	$1_2 2_2$, asym	180(0)	201(2)	187(2)	205(1)	0.16
	Average	180(0)	201(2)	187(1)	205(1)	
$Li_4[Mn(III)_3(OH_2)_3]$	$1_3 2_1$	226(0)	204(0)	190(1)	221(0)	0.15
	$1_1 2_3$	225(0)	200(2)	192(2)	222(1)	0.00
	$1_2 2_2$, sym	226(0)	202(3)	191(1)	221(0)	0.21
	$1_2 2_2$, asym	225(0)	202(2)	191(2)	221(0)	0.04
	Average	225(1)	202(2)	191(1)	221(1)	
	Exp.[b]	217(2)	194(1)	192(2)	225(3)	
$Li_7[Mn(II)_3(OH_2)_3]$	$1_3 2_3 5_1$	225(0)	221(0)	211(0)	230(0)	0.02
	$1_3 2_3 6_1$	227(0)	213(0)	219(0)	232(0)	0.00
	Average	226(1)	217(4)	215(4)	231(1)	
	Exp.[b]	217(0)	201(1)	198(1)	233(0)	

[a] Mn-O_t bonds to the terminal ligand, H_2O for Mn(II) and Mn(III), OH for Mn(IV), Mn-OH bonds to the bridging OH groups, Mn-O_W bonds to the O centers connecting Mn and W, Mn-O_{Si} bonds to the O centers of the central Si tetrahedron.
b Ref. [16].

structural parameters of optimized structures, representing isomers of various Li arrangements, together with the total energy differences E_{rel} relative to the most stable isomer. Bond lengths are averaged over all incidents: Mn-O_t and Mn-O_{Si} are averaged over 3 values, Mn-OH and Mn-O_W over 6 values; standard deviations are given in parentheses. For each oxidation state of Mn, the relative energies among the isomers differ at most by 0.23 eV. This suggests that all these arrangements may coexist in solution. For the POM with Mn(IV) the most favorable structure is the one with the Li arrangement $1_3 2_1$; Li prefers the site 1, close to Mn centers (Fig. 2). The least favorable structure is the one with the Li arrangement $1_1 2_3$ where three Li cations occupy sites of type 2 and only one a site of type 1. For the POM with Mn(III) the energetic preference is opposite: arrangement $1_1 2_3$ is favored over $1_3 2_1$ (Table 2). Interestingly, both arrangements studied, $1_3 2_3 5_1$ and $1_3 2_3 6_1$ for the POM with Mn(II), are very close in energy, differing by only 0.02 eV in total energy. Although a single Li cation clearly favors site 5 over site 6, the two structures with seven Li cations are essentially degenerate in energy.

The arrangement of the Li counterions only slightly affects the Mn-O distances of the POMs with Mn in oxidation states (IV) and (III). For $Li_4[Mn(IV)_3(OH)_3]$ the average Mn-O_t bond lengths are not affected by the Li arrangement; it is 180 pm without any standard deviation for all arrangements studied. The average values of Mn-O_W and Mn-O_{Si} do not exceed 2 pm among the various arrange-ments of the counterions (Table 2), and the corresponding standard deviations are at most 2 pm. The average Mn-O_W distances of the O bridges to the W centers vary in a similarly narrow margin, from 186(1) pm to 188(2) pm; the Mn-O_{Si} bonds are equally stable, between 204(0) and 205(1) pm.

The most sensitive structure parameter of the Keggin ions is the Mn-OH bond to the bridging OH group. It is calculated at 202(1) pm for $1_3 2_1$ and at 198(2) pm for $1_1 2_3$ (Table 2). The bridging OH ligands coordinate to Li cations when they occupy sites 1. Therefore, changes in the average Mn-OH bonds reflect some bond competition. When 3 Li ions occupy sites 1 and coordinate to all three bridging OH, the corresponding average Mn-OH is 202 1 pm. In contrast, when only one site 1 is occupied, together with the three sites 2, the average Mn-OH distance is 4 pm shorter, 198 2 pm (Table 2). For the arrangements $1_2 2_2$, both sym and asym, when two Li^+ occupy sites 1, the average Mn-OH results in an intermediate value, 201(2) pm. Assuming that all arrangements are present in solution to similar amounts allows one to average over all Li arrangements. The resulting averaged bond distances are also given in Table 2. The largest standard deviation, 2 pm, is again calculated for the Mn-OH bonds.

Similar trends as for Mn(IV) are obtained for the system $Li_4[Mn(III)_3(OH_2)_3]$. None of the standard deviations exceeds 3 pm (Table 2). The average values of Mn-O_W and Mn-O_{Si} vary by 2 pm at most. The largest deviations again result for Mn-OH bond, 4 pm (Table 2), between the Li arrangements $1_3 2_1$ and $1_1 2_3$, due to bond competition as just discussed. In contrast to Mn(IV), the Mn-O_t distance of the Mn(III) systems is notably larger, varying from 225
(0) pm to 226(0) pm. This is a consequence of the fact that, for Mn (III), the distance Mn-O_t represents a coordinative bond of an aqua ligand whereas for Mn(IV) this distance is a bond to an OH ligand. The weaker (and longer) Mn-O_t bonds to H_2O ligands are more prone to vary, compared to the stronger (and shorter) Mn-O_t bonds to OH ligands.

The averaged Mn-OH and Mn-O_W bond lengths also increase when Mn is reduced from (IV) to (III), but only slightly, by 1 pm and 4 pm, respectively (Table 2). Interestingly, the averaged Mn-O_{Si} distance increases by 16 pm when Mn is reduced from (IV) to (III). It is one of the longest Mn-O bonds and therefore more prone to react to the change of Mn charge. When the charge of the Mn center is decreased from +4 to +3 (reduction), this coordinative Mn-O_{Si} bond to the central $[SiO_4]^4$ fragment naturally gets longer.

Structural changes due to different Li^+ arrangements are more pronounced for $Li_7[Mn(II)_3(H_2O)_3]$. While the Mn-O_t and Mn-O_{Si} bond lengths vary by 2 pm, the Mn-OH and Mn-O_W change significantly, when only one Li^+ changes its position, from site 5 to site 6. The distance Mn-OH is 8 pm longer for the arrangement $1_3 2_3 5_1$, compared to $1_3 2_3 6_1$. The bridging OH moieties for Li^+ occupying site 5, exhibit longer Mn-OH distances for $1_3 2_3 5_1$. The average distance Mn-O_W shows the opposite trend; it is shorter for the arrangement $1_3 2_3 5_1$, 211(0) pm, and 8 pm longer for $1_3 2_3 6_1$ (Table 2). Averaging over these Li arrangements results in the largest standard deviations, 4 pm for the distances Mn-OH and Mn-O_W; the distances Mn-O_t and Mn-O_{Si} exhibit standard deviations of 1 pm.

All calculated Mn-O distances, except Mn-O_t, increase when Mn is reduced from (III) to (II). Averaged Mn-OH, Mn-O_W, and Mn-O_{Si} increase by 15 pm, 24 pm, and 10 pm, respectively (Table 2). The charge of the Mn centers decreases from +3 e to +2 e under the reduction (III/II) and one can expect Mn-O bonds to elongate due to lower Coulomb attraction. However, the Mn-O_t distance to the

terminal OH_2 ligands almost does not change in this situation; it is 225 1 pm on average for the POM with Mn(III) and 226 1 pm for the POM with Mn(II). The same trend is observed in experiment (discussed below) [16]. The reason for such structural invariance is unclear.

To identify potential effects of various exchange-correlation functionals on the structure parameters of the POMs, we analyzed and compared the structural parameters obtained from calcu-lations with the functionals B3LYP, PBE0, and TPSSh; see Table S1 of the Supplementary Data (SD). Overall, the effect of the exchange-correlation functional on the structures is rather small. Average bond lengths vary at most by 3 pm. PBE and B3LYP results are slightly longer, by 1–2 pm, than the results of PBE0 and TPSSh calculations. Previous studies found that experimental structural parameters of Keggin-type polyoxometalates are best reproduced in PBE0 calculations [17,18]. However, the average absolute errors of the functionals PBE0, B3LYP, and PBE, do not exceed 3 pm [17,18]. In conclusion, calculations with GGA and various hybrid func-tionals yield rather similar structural parameters, in contrast to the resulting energy characteristics [17,18]. In consequence, we refrain from comparing here the structural results for the POMs calculated with hybrid methods; for details, see the SD.

Tri-Mn-substituted Keggin ions with Mn in oxidation states (II) and (III) were synthesized and characterized by Al-Oweini et al. [16]. The experimentally determined bond lengths are also given in Table 2, for comparison. For $Li_4[Mn(III)_3(OH_2)_3]$, the distances Mn-O_W and Mn-O_{Si} are very well reproduced (Table 2), while calculated distances Mn-O_t and Mn-OH are overestimated by 8 pm at the PBE level. For $Li_7[Mn(II)_3(OH_2)_3]$ only the Mn-O_{Si} distance is well reproduced. The calculated Mn-O_t distance are 9 pm longer than the corresponding experimental value. The distances Mn-OH and Mn-O_W deviate even more from experiment; they are calculated 16–17 pm longer (Table 2). Note that the experiment examined crystal structures where several POMs are linked to each other by counterions, K^+ and Na^+ [16]. In our model calculations we addressed systems in aqueous solution, employing a polarizable continuum method to represent the solvent; no interaction among POMs is taken into account. Not unexpectedly, only Mn-O_{Si} bonds are well reproduced for both types of POMs; these bonds are not directly affected by the electrolyte surrounding the POMs.

However, the calculated distances reproduce trends of experi-mental structural parameters that occur upon reduction Mn(III/II). For such a reduction, the experimental distances Mn-O_t does not change, just as the calculated Mn-O_t values which change by 1 pm only. Mn-O_{Si} bond lengths increase due to Mn reduction by 8 pm in experiment and by 10 pm in our calculations (Table 2). The experimental distances Mn-OH and Mn-O_W increase by 6–7 pm, the calculated values increase by 20 pm (Table 2).

Thus, our analysis of structural parameters of POMs with Mn in various oxidation states has shown that most Mn-O bonds do not vary much among different Li arrangements. The exchange-correlation approximation also hardly affects the Mn-O bonds, by 2–3 pm on average. Our findings agree with those of earlier studies on POMs [17,18] where similarly small variations of structure parameters had been determined for different ex-change-correlation functionals. This similarity did not carry over to calculated chemical shifts [18] and energies of frontier molecular orbitals [17]. The present comparison with experimental crystal structure data showed that the structural changes due to Mn(III/II) reduction are well reproduced by the model calculations. However, most calculated Mn-O distances are overestimated compared to experiment, with the exception of the Mn-O_{Si} bonds that are not directly affected by the counterions and the surrounding solvent. These latter findings may be a harbinger for the need to strive ultimately for a more sophisticated modeling of the interaction of a POM with its electrolyte environment.

Table 3
Standard reduction potentials U^0_{red} vs NHE (eV) for the redox processes Mn(IV/III) and Mn(III/II), estimated from Eq. (6), calculated at various levels of theory: PBE, B3LYP, PBE0, and TPSSh. Also shown are the average values $<U^0_{red}>$ over the various Li arrangements. For the site designations, see Figs. 2 and 3.

	Ion configuration	PBE	TPSSh	B3LYP	PBE0
Mn(IV/III)	1_32_1	0.86	1.25	1.66	1.78
	1_12_3	0.81	1.17	1.60	1.71
	1_22_2, sym	0.85	1.21	1.63	1.74
	1_22_2, asym	0.85	1.21	1.63	1.75
	$<U^0_{red}>$	0.84 0.03	1.21 0.04	1.63 0.04	1.74 0.04
Mn(III/II)	1_32_1	0.44	0.78	1.12	1.24
	1_12_3	0.33	0.65	1.00	1.11
	1_22_2, sym	0.43	0.70	1.05	1.16
	1_22_2, asym	0.36	0.68	1.04	1.15
	$<U^0_{red}>$	0.39 0.07	0.70 0.08	1.05 0.07	1.16 0.08

3.3. Standard reduction potentials

Having clarified structural aspects of the tri-Mn-substituted Keggin ion and its electrolyte environment, we now turn to determining electrochemistry characteristics and how they are affected by the Li arrangements. From the reaction free energy change DG of the reaction

$$POM + n\,e \;!\; POM^n \quad , \qquad (5)$$

we calculate the standard reduction potential

$$U^0_{red} \;\; \frac{DG}{\;\;} \;\; ¼ \; nF \; UðNHEÞ \qquad ð6Þ$$

Here, F is the Faraday constant and n the number of electrons transferred, n = 3 in the present case. We determine reduction potentials with respect to the normal hydrogen electrode (NHE), with the reduction potential U(NHE) = 4.28 eV [53]. Table 3 provides the values U^0_{red} vs NHE for the reduction steps Mn(IV/III) and Mn(III/II), assuming various arrangements of the Li counterions and for the exchange-correlation functionals selected for this study.

Similar to the structure characteristics, also the standard reduction potentials are rather similar for all Li arrangements studied if evaluated at the same level of theory (Table 3). However, these values vary notably among the different exchange-correla-tion approximations used, in contrast to the calculated structural parameters. At a given level of theory, the calculated values U^0_{red} for the reduction Mn(IV/III) vary by up to 0.08 eV among the Li arrangements examined. The standard reduction potentials U^0_{red} evaluated for the reduction step Mn(III/II) vary somewhat more, by up to 0.11–0.13 eV (Table 3). The largest value U^0_{red} is always calculated for the counterion arrangement 1_32_1, and the lowest one for the arrangement 1_12_3; the value U^0_{red} obtained with the two arrangements 1_22_2 lie in between and are very similar (Table 3). In view of the rather small deviations, one may also discuss average values $<U^0_{red}>$ of the standard reduction potentials over the various Li arrangements studied (Table 3).

With the pure GGA functional PBE, one estimates the lowest values $<U^0_{red}>$ = 0.84 0.03 eV for the reduction Mn(IV/III) (Ta-ble 3). A notably larger value $<U^0_{red}>$ = 1.21 0.04 eV is calculated using the hybrid functional TPSSh. The two other hybrid func-tionals, B3LYP and PBE0, yield even larger values $<U^0_{red}>$, 1.63 0.04 eV and 1.74 0.04 eV, respectively (Table 3). Thus, one finds an interesting trend: the value $<U^0_{red}>$ increases with the fraction of the exact exchange in the functional. The pure GGA functional PBE does not contain any exact exchange and yields the lowest reduction potential. The hybrid functionals TPSSh, B3LYP, and PBE0 feature 10%, 20%, and 25% of exact exchange, respectively.

The corresponding averages $\langle U^0_{red} \rangle$ of the reduction potentials increase in the same order (Table 3).

A similar trend in $\langle U^0_{red} \rangle$ is observed for the reduction step Mn (III/II). The PBE calculations yield the lowest value, $\langle U^0_{red} \rangle$ = 0.39 0.07 eV. The results for the hybrid functionals again increase in the order TPSSh, B3LYP, and PBE0, namely 0.70 0.08 eV, 1.05 0.07 eV, and 1.16 0.08 eV, respectively (Table 3). This effect of the amount of exact exchange on calculated redox potentials has previously been noted for the Mn center of superoxide dismutase [19]; in that case, the hybrid B3LYP functional yields a redox potential that is 0.6 eV larger than the corresponding PBE result [19].

The standard oxidation potential U^0_{ox} can be calculated in an analogous fashion:

$$POM ! n e + POM^{n+} \quad (7)$$

$$U^0_{ox} = \frac{DG}{nF} - U_{NHE} \quad (8)$$

To facilitate comparison with experiments, more precisely with the measured reversible half-wave potential U_{rev}, one has to take the average of U^0_{red} and U^0_{ox}. As test, we calculated U^0_{ox} for the oxidation Mn(III/IV) of the Li arrangement $1_3 2_1$: 1.96 eV for PBE and 2.80 eV for B3LYP. Therefore, the estimated reversible half-wave potential U_{rev} for the redox process Mn(IV/III) is 1.41 eV at the PBE level and 2.23 eV at the B3LYP level. The experimental value changes from 0.85 eV to 1.05 eV for pH values ranging from 6.0 to 4.2 [13]. Both results, from PBE and B3LYP calculations overesti-mate the experimental values quite notably, by at least 0.4 eV and 1.2 eV, respectively.

The computational approach just described for estimating redox potentials is rather straightforward, but it has notable disadvantages. Foremost, the computational procedure does not account for any pH dependence. First, U^0 depends on solvation energies of the charged species as can be seen from Eqs. (5) and (7). We used the COSMO approach for calculating free energies of solvation. The accuracy of this method is known to deteriorate for systems with high molecular charge (3 e in our case) due to incomplete description of electrostatics, hydrogen bonds, disper-sion, and other solvation effects [50]. Thus, inaccuracies in DG_{solv} calculations can be a limiting factor for a quantitative prediction of redox potentials, when highly charged species are involved. Another factor affecting the accuracy of calculated redox potentials is the mechanism of the redox reaction, e.g., a protonation of the reduced POMs, or a deprotonation of the oxidized species. Taking this into account will also introduce a pH dependence which is missing so far in modeling but seen in experiment [13]. The next section, focusing on a comparison of calculated and measured redox potentials, describes alternative ways for estimating the reversible potential U_{rev} as measured in cyclic voltammetry.

3.4. Comparison with experiment

The measured reversible half-wave redox potentials, E_{rev}, [13] (we use E to distinguish experimental potentials from calculated ones to which we refer as U) do not only depend on the electron transfer itself, but also on other processes occurring simulta-neously in the solution. For the reduction Mn(IV/III), the proton transfer accompanying the electron transfer has to be taken into account, while for the reduction Mn(III/II) the cation transfer should be accounted for. To include the redox mechanism in the model, we take the Gibbs free energies of the full reduction reactions, Eqs. (1) and (2), that directly include proton/cation transfer. We use these free energy values in Eq. (6) to obtain the standard reduction potentials, U^0_{red}. Eqs. (1) and (2) correspond to the reduction process; the corresponding oxidation process can be described by the reversed equations. Then, with Eq. (8), one obtains the standard oxidation potential U^0_{ox}. Yet, the correspond-ing Gibbs free energies differ only by the sign which cancels out in Eq. (8). Therefore the standard U^0_{red} and U^0_{ox} calculated from the full reactions will be the same. Therefore, we drop the subscripts and simply write U^0. Next, we apply the Nernst equation, which relates the cell potential to the standard potential and to the activities of the electroactive species [54]:

$$U = U^0 - \frac{RT}{nF} \ln Q \quad (9)$$

Here, U is the redox potential at the temperature T of interest, U^0 is the standard redox potential, Q is the reaction quotient, i.e., the ratio of activities of products and reactants of the reaction; activities are commonly replaced by concentrations [54]. Recall that the half-wave potential E_{rev} measured by cyclic voltammetry corresponds to the condition, at which the concentrations of oxidants and reductants are equal; to the redox potential at this condition, we refer to as U_{rev}. We will first discuss the redox process Mn(III/II). Subsequently, we will turn to the process Mn(IV/III).

When considering Eq. (2) to describe the redox process Mn(III/ II), one should recall that the experimental concentration of Li^+ is 1 M [13]. Therefore, Q = 1 when the concentration of the oxidant is equal to the concentration of the reductant and the Nernst correction vanishes. Hence, for Mn(III/II), U^0 represents the computationally estimated U_{rev} and can be directly compared to the experimentally measured value E_{rev}.

In Table 4 we present this direct comparison of the calculated U_{rev} to the measured results for the redox process Mn(III/II), for all Li ion configurations in the initial as well as the final state of Eq. (2). For each functional, the calculated redox potentials U_{rev} vary at most by 0.1 eV, from 0.28 to 0.38 eV for PBE, from 0.63 to 0.70 eV for TPSSh, from 0.99 to 1.06 eV for B3LYP, and from 1.12 to 1.20 eV for PBE0 (Table 4). Thus, for a chosen exchange-correlation potential, the Li arrangement does not affect the value U_{rev} in a significant way. Not unexpectedly (Section 3.3), the PBE functional yields the lowest average value for the reversible potential, U_{rev} = 0.32 0.04 eV. The largest such value was calculated with the PBE0 functional, U_{rev} = 1.16 0.03 eV. The functionals TPSSh and B3LYP yield intermediate values of U_{rev}, 0.66 0.02 and 1.02 0.02 eV, respectively. The best agreement with the measured redox potential E_{rev} of 0.65 eV [13] is obtained with the functional TPSSh (Table 4). The PBE results underestimate the experimental result by 0.3 eV, while both B3LYP and PBE0 results overestimate the experiment by 0.4–0.5 eV (Table 4).

The situation is different in the case of the redox process Mn(IV/ III) because Q for the reaction described in Eq. (1) deviates from 1 due to the variable proton concentration (pH of the solution). For

Table 4
Calculated reversible redox potentials[a] U_{rev} vs. NHE (eV) for the cation-coupled redox process Mn(III/II), estimated from Eqs. (2) and (6), for results obtained at various levels of theory: PBE, TPSSh, B3LYP, and PBE0.

Initial configuration[b]	PBE	TPSSh	B3LYP	PBE0	Exp.[c]
$1_3^1 2$	0.32, 0.34	0.68, 0.70	1.04, 1.06	1.17, 1.20	
$1_1^2 3$	0.28, 0.30	0.63, 0.65	0.99, 1.01	1.12, 1.14	
$1_2 2_2$, sym	0.36, 0.38	0.66, 0.67	1.01, 1.03	1.15, 1.17	
$1_2 2_2$, asym	0.29, 0.31	0.65, 0.66	1.00, 1.03	1.14, 1.16	
$\langle U_{rev} \rangle$[d]	0.32 0.04	0.66 0.02	1.02 0.02	1.16 0.03	0.65

a The first value of each entry refers to the Li arrangement $1_3 2_3 5_1$ in the final state of Eq. (2), $Li_7[Mn(II)_3(OH_2)_3]$, the second value to the Li arrangement $1_3 2_3 6_1$; see Figs. 2 and 3.

b Initial arrangement of the Li counterions.

c Ref. [13].

d Average result of all Li arrangements studied, including the standard deviation.

estimating the reversible redox potential U_{rev} of the proton-coupled redox process, we consider a step-wise addition of protons [55]:

$$Li_4[Mn(IV)_3(OH)_3] + 3e \rightarrow Li_4[Mn(III)_3(OH)_3]^3 \quad (10a)$$

$$Li_4[Mn(III)_3(OH)_3]^3 + H^+ \rightarrow Li_4[Mn(III)_3(OH_2)(OH)_2]^2 \quad (10b)$$

$$Li_4[Mn(III)_3(OH_2)(OH)_2]^2 + H^+ \rightarrow Li_4[Mn(III)_3(OH_2)_2(OH)] \quad (10c)$$

$$Li_4[Mn(III)_3(OH_2)_2(OH)] + H^+ \rightarrow Li_4[Mn(III)_3(OH_2)_3] \quad (10d)$$

Eq. (10a) describes the standard reduction potential U^0_{red}, Eqs. (10b), (10c), and (10d) describe the reversed dissociation reactions of the possible reductant complexes formed in each of the three steps; the latter are represented by the dissociation constants K_1, K_2, K_3, respectively. The measured reversible redox potential E_{rev} [13] corresponds to the condition at which the concentrations of oxidized, [Ox], and reduced, [Red], species are equal. From Eq. (10a), $Ox = Li_4[Mn(IV)_3(OH)_3]$, $Red = Li_4[Mn(III)_3(OH)_3]$. The pH of the solution de nes the degree of protonation of the reduced complex. At different pH of the solution there are various reduced complexes, namely Red^3 , $RedH^2$, $RedH_2$, $RedH_3$. Therefore, in experiment the reversible half-wave redox potential E_{rev} for the process Mn(IV/III) is measured at the condition where

$$[Ox] = [Red]_{total} = [Red^3] + [RedH^2] + [RedH_2] + [RedH_3]. \quad (11)$$

Therefore, one has for the calculated reversible potential U_{rev} of the redox process Mn(IV/III) [55]:

$$U_{rev} = U^0 + \frac{RT}{3F} \ln\left(1 + \frac{[H^+]}{K_1} + \frac{[H^+]^2}{K_1K_2} + \frac{[H^+]^3}{K_1K_2K_3}\right) \quad (12)$$

Table 5 compares the corresponding computationally estimated values U_{rev} to the measured results E_{rev} [13]. The corresponding calculated dissociation constants are provided as SD.

First of all, all exchange-correlation functionals examined reproduce the pH dependence. At pH = 4.2 the computed redox potential is 0.1 eV higher than the corresponding redox potential at pH = 6 (Table 5). The corresponding measured difference between the two E_{rev} at pH = 4.2 and 6 is 0.2 eV [13]. Different from Mn(III/II), where the hybrid exchange-correlation functional TPSSh shows the best agreement with experiment, for Mn(IV/III) the PBE results agree best with experiment. TPSSh overestimates the measured potentials by 0.6 eV, and B3LYP and PBE0 by 1 eV (Table 5). This is in contrast to the common expectation of a better performance of the hybrid DFT methods, compared to the pure GGA approach. Predicting the accuracy of DFT methods for particular systems is difficult [56,57]. For the first-row transition metals, it has been shown [58] that pure GGA and hybrid functionals tend to deviate from experiment in opposite directions, e.g. for calculated bond lengths and, more importantly in the present context, for ionization potentials and dipole moments. Roy et al. [59] calculated redox potentials for various redox couples for a series of small transition metal compounds of the first-, second-, and third-row elements. They also obtained better alignment with experiment for the pure GGA functionals BP86 and PBE, $R^2 = 0.97$; the hybrid methods yielded $R^2 = 0.83$ only [59]. These authors suggested that the better performance of pure GGA may be due to error cancellation of the additional solvent and/or metal electrode surface effects taking place in experiment [59].

Table 5
Calculated reversible redox potentials U_{rev} vs. NHE (in eV) for the proton-coupled redox process Mn(IV/III), estimated from Eq. (12), for results obtained at various levels of theory: PBE, TPSSh, B3LYP, PBE0. The numbers are given for Li arrangement 1_32_1.

	PBE	TPSSh	B3LYP	PBE0	Exp.[a]
Mn(IV/III)					
U_{rev}, pH 4.2	1.05	1.61	1.91	2.12	1.05
U_{rev}, pH 6	0.98	1.51	1.81	2.01	0.85

[a] Ref. [13].

However, the better performance of a pure GGA functional, compared to the hybrid methods, may be fortuitous as other approximations may affect the computational results, e.g., the solvation model. As mentioned in Section 3.3, solvation energies of highly charged species may suffer from larger uncertainties. Besides the solvation model itself, an accurate description of the electrolyte structure can be also crucial. The popular COSMO approach may not suffice for reflecting the solvation effects on the Li cations; rather, some water molecules may have to be explicitly described. Using the COSMO method for calculating redox potentials of the aqua complexes of Ru(III/II) and Os(III/II), Srnec et al. indicated [60] that in that case solvation energies may be quite inaccurate (up to 1 eV for the Ru complexes) unless the second solvation sphere (12–14 H_2O molecules) is taken explicitly into account [60]. In the present case of POMs, such models will be computationally quite demanding.

We probed this effect by introducing one explicit water molecule for each Li cation of the arrangement 1_32_1 of the POM models for Mn(IV) and Mn(III), and the arrangement $1_32_35_1$ of the POM model for Mn(II). For the process Mn(III/II) the reversible redox potential U_{rev} was calculated at the PBE level at 0.19 eV as compared to 0.32 eV for the corresponding model without explicit solvation. Similarly, at the TPSSh level, the calculated value U_{rev} was reduced to 0.58 eV compared to 0.68 eV for the non-solvated model. While the explicit solvation decreases the calculated reversible potential for Mn(III/II) by 0.1 eV, the TPSSh result still compares very well with the experimental result $E_{rev} = 0.65$ eV [13]. For Mn(IV/III) the calculated U_{rev} decreased by 0.06 eV at the PBE level and by 0.04 eV at the TPSSh level. These rather simple test calculations suggest that the effect of the second solvation shell of the POM is larger for Mn(III/II) than for Mn(IV/III). For Mn(III/II) the initial and final structures of the near field electrolyte change considerably; three Li^+ ions are added to the structure when Mn(III) is reduced to Mn(II). Therefore, a change in the description of the solvation effects, namely adding explicit water molecules directly in the quantum-chemical model, can noticeably affect the calculated redox potential. As for the redox process Mn(IV/III) the electrolyte environment does not change in such a drastic way, the number of Li^+ ions near the POM does not change under reduction/oxidation. Therefore, one expects that the present model is more appropriate for Mn(IV/III) than for Mn(III/II).

In the present models we represented Li^+ ions as inner-sphere adsorbates on the surface of the POM, and we chose the strongest adsorption sites. This is yet another simplification of the electrolyte environment near a POM. In solution, the cations may occupy over time different sites and they may even be adsorbed in outer-sphere fashion. To explore this aspect, we carried out an additional test, examining how the distance between Li cations and the surface of the POM may affect the redox potentials. For this purpose, we moved the Li^+ ions of the optimized 1_32_1 arrangement by 50 pm along the Si-Li axes away from the surface of the POM. For these structure, we calculated the reversible redox potentials U_{rev} at the PBE level. For Mn(IV/III), the value decreased from 1.05 eV to 1.01 eV and, for Mn(III/II), from 0.32 eV to 0.06 eV. This model consideration indicates once again that a correct description of the electrolyte is crucial for calculating redox potentials, especially for cation-coupled electron transfer where the structure of near field electrolyte changes notably.

4. Conclusions

We studied computationally the tri-Mn-substituted W-based Keggin ion. By means of DFT calculations, we determined the structure of these polyoxometalates (POMs), focusing on three systems with all Mn centers uniformly in the same oxidation state, (IV), (III), and (II). To neutralize the highly charged POMs, we followed the experiment [13,16] and designed model systems with the POMs in an aqueous electrolyte containing Li^+ ions. Therefore, we added an appropriate number of Li cations to the quantum chemical models, placing them near the surface of the POM in various arrangements. Hence, we added four Li cations to the models of $[Mn(IV)_3(OH)_3]^4$ and $[Mn(III)_3(OH_2)_3]^4$ as well as seven cations to the model of $[Mn(II)_3(OH_2)_3]^7$. We tested a pure GGA exchange-correlation functional and several hybrid DFT approaches. As a result, we found out that, for each of the Mn oxidation states studied, the main structural parameters of the POMs were not affected by the Li arrangement nor the exchange-correlation functional. While the calculated structural parameters were found to overestimate some of the experimental interatomic distances, the calculations successfully reproduced the geometric trends [16] upon reduction of the Mn centers from (III) to (II).

Similarly, the standard reduction potentials were found to be not sensitive to the Li arrangement, but the calculated results depend strongly on the exchange-correlation functional. The lowest standard reduction potentials were determined with the pure GGA functional, PBE. The three hybrid functionals tested, TPSSh, B3LYP, and PBE0, yield higher reduction potentials which increase (in that order) with the contribution of exact exchange in the hybrid functional.

For comparison with experiment we used the full redox reactions, including the transfer of protons or cations coupled with the electron transfer. For the cation-coupled redox process Mn(III/ II), the reversible redox potential U_{rev} calculated with TPSSh compares best with experiment. The GGA functional PBE yields a result that underestimates the measured value of E_{rev} [13] by 0.3 eV, while results of B3LYP and PBE0 overestimate it by 0.5 eV. For the proton-coupled electron transfer of the redox process Mn(IV/III), we corrected the standard reduction potential using the dissociation constants of the protonated POMs and the Nernst equation. The resulting U_{rev} values reproduce the experi-mental pH dependence [13]. Surprisingly, the PBE result shows the best agreement with experiment, while the U_{rev} results of the hybrid functionals explored notably overestimate experimental E_{rev} by 0.6–1 eV.

The good performance of the pure GGA approach compared to hybrid methods seems to be due to fortuitous error cancellation [59]. Another source of uncertainty is the solvation model that may lead to smaller redox potentials if a more realistic description based on explicit solvation is included in the quantum chemical model. One expects that models with such an improved descrip-tion of solvation (e.g., by solvated counterions) affect more noticeably the calculated U_{rev} values for Mn(III/II) than for Mn (IV/III) because the near field electrolyte changes more notably in the former case as the number of Li cations close to the POM varies during the reduction Mn(III/II).

Obtaining accurate results for redox potentials of POMs apparently is still a challenge for computational chemistry methods. Preliminary simple model studies indicated that the structure of the electrolyte near a POM, especially the distances to the counterions as well as the screening of these ions by water molecules, may be essential for achieving quantitative agreement between theoretical and experimental data. The results of the present study point to a crucial need for a more refined atomistic representation of the (average) effective potential due to the electrolyte environment. The approximate nature of the effective potential used here, although going beyond a straightforward polarizable continuum model, seems to be a major reason for the limited accuracy of the calculated redox potentials. Experimental conditions, not reflected by the present type of computational models, may also affect the calculated redox properties, e.g., the nature of the electrolyte and the working electrode. On the computational side, uncertainties remain regarding the choice of the exchange-correlation functional [57,58], and the description of the electrolyte. In the latter case, one may have to resort to more elaborate methods, e.g., by describing the electrolyte via a solution of the generalized Poisson-Boltzmann equation. Here, recent advances for computational methods seem to be promising [61–64].

Alternatively, one may use an internal reference, either from experiment or a calculation, that allows quantitative predictions of redox potentials with standard deviations that are comparable to typical experimental errors of cyclic voltammetry [20,31]. Results of this work, therefore, besides being pioneering, can be used further as a reference.

In summary, the present study confirms the experimentally determined electrochemical behavior of a tri-Mn-substituted Keggin ion. This computational work provides a protocol for calculating redox potentials that, to a certain degree, can be compared to measured redox potentials of other POMs. However, the present results also show where the computational approach has to be improved in order to achieve a more reliable modelling.

Acknowledgements

The authors are grateful to Jochen Friedl and Ulrich Stimming for many insightful discussions about electrochemistry in general and the electrochemical properties of POMs in particular. We also thank Ulrich Kortz for showing us many facets of the world of POMs. The authors acknowledge a generous grant of computing resources by the Gauss Centre for Supercomputing (www.gauss-centre.eu), provided on the SuperMUC platform of Leibniz Super-computing Centre Garching (www.lrz.de).Appendix A. Supple-mentary data

Supplementary data associated with this article can be found, in the online version, at http://dx.doi.org/10.1016/j. electacta.2017.02.046.

References

[1] U. Kortz, Polyoxometalates, Eur. J. Inorg. Chem. (2009) 5056.
[2] U. Kortz, A. Müller, J. van Slageren, J. Schnack, N.S. Dalal, M. Dressel, Polyoxometalates: Fascinating structures, unique magnetic properties, Coord. Chem. Rev. 253 (2009) 2315–2327.
[3] J.F. Keggin, Structure of the molecule of 12-phosphotungstic acid, Nature 131 (1933) 908–909.
[4] J.F. Keggin, The structure and formula of 12-phosphotungstic acid, Proceedings of the Royal Society of London. Series A 144 (1934) 75–100.
[5] C.L. Hill, Introduction: Polyoxometalates – Multicomponent molecular vehicles to probe fundamental issues and practical problems, Chem. Rev. 98 (1998) 1–2.
[6] M. Sadakane, E. Steckhan, Electrochemical properties of polyoxometalates as electrocatalysts, Chem. Rev. 98 (1998) 219–237.
[7] M.T. Pope, Heteropoly and isopoly oxometalates, Springer-Verlag, Berlin, 1983.
[8] H. Wang, S. Hamanaka, Y. Nishimoto, S. Irle, T. Yokoyama, H. Yoshikawa, K. Awaga, In operand X-ray absorption fine structure studies of polyoxometalate molecular cluster batteries: polyoxometalates as electron sponges, J. Am. Chem. Soc. 134 (2012) 4918–4924.
[9] Y. Nishimoto, D. Yokogawa, H. Yoshikawa, K. Awaga, S. Irle, Super-reduced polyoxometalates: excellent molecular cluster battery components and semipermeable molecular capacitors, J. Am. Chem. Soc. 136 (2014) 9042–9052.
[10] R.J. Liu, G.J. Zhang, H.B. Cao, S.J. Zhang, Y.B. Xie, A. Haider, U. Kortz, B.H. Chen, N. S. Dalal, Y.S. Zhao, L.J. Zhi, C.X. Wu, L.K. Yan, Z.M. Su, B. Keita, Enhanced proton and electron reservoir abilities of polyoxometalate grafted on graphene for high-performance hydrogen evolution, Energy Environ. Sci. 9 (2016) 1012– 1023.

[11] P. Leung, X. Li, C. Ponce de León, L. Berlouis, C.T.J. Low, F.C. Walsh, Progress in redox flow batteries, remaining challenges and their applications in energy storage, RSC Advances 2 (2012) 10125–10156.

[12] H.D. Pratt III, N.S. Hudak, X. Fang, T.M. Anderson, A polyoxometalate flow battery, J. Power Sources 236 (2013) 259–264.

[13] J. Friedl, R. Al-Oweini, M. Herpich, B. Keita, U. Kortz, U. Stimming, Electrochemical studies of tri-manganese substituted Keggin Polyoxoanions, Electrochim. Acta 141 (2014) 357–366.

[14] M. Sadakane, E. Steckhan, Co-solvent effects on the redox potentials of manganese-substituted alpha-Keggin-type silicon polyoxotungstate $K_6SiW_{11}O_{39}Mn(H_2O)$): First electrochemical generation of the Manganese(V) redox system in an aqueous environment, Acta Chem. Scand. 53 (1999) 837– 841.

[15] T. Janoschka, N. Martin, U. Martin, C. Friebe, S. Morgenstern, H. Hiller, M.D. Hager, U.S. Schubert, An aqueous, polymer-based redox-flow battery using non-corrosive, safe, and low-cost materials, Nature 527 (2015) 78–81.

[16] R. Al-Oweini, B.S. Bassil, J. Friedl, V. Kottisch, M. Ibrahim, M. Asano, B. Keita, G. Novitchi, Y. Lan, A. Powell, U. Stimming, U. Kortz, Synthesis and characterization of multinuclear manganese-containing tungstosilicates, Inorg. Chem. 53 (2014) 5663–5673.

[17] H.-N. Wu, J. Wang, H. Li, N.-N. Ma, T. Zhang, S.-Q. Shi, L.-K. Yan, Z.-M. Su, Structure and Frontier Molecular Orbital (FMO) energies of a-Keggin-type polyoxometalate $[PW_{12}O_{40}]^3$: A systematical study with different functionals of density functional theory, Comp. Theor. Chem. 1089 (2016) 28–34.

[18] R. Sharma, J. Zhang, C.A. Ohlin, Predicting ^{17}O NMR chemical shifts of polyoxometalates using density functional theory, Phys. Chem. Chem. Phys. 18 (2016) 8235–8241.

[19] J. Heimdal, M. Kaukonen, M. Srnec, L. Rulíšek, U. Ryde, Reduction potentials and acidity constants of Mn superoxide dismutase calculated by QM/MM free-energy methods, ChemPhysChem 12 (2011) 3337–3347.

[20] S.J. Konezny, M.D. Doherty, O.R. Luca, R.H. Crabtree, G.L. Soloveichik, V.S. Batista, Reduction of systematic uncertainty in DFT redox potentials of transition-metal complexes, J. Phys. Chem. C 116 (2012) 6349–6356.

[21] N. Ma, S. Li, L. Yan, W. Wang, Y. Qiu, G. Zhang, Electronic properties of polyoxometalate derivatives $[(C_2B_9H_{11})\ M'M_5O_{18}]^n$ (M' = Ti^{IV}, Mo^{VI}, W^{VI}; M = Mo^{VI}, W^{VI}): Protonation, electronic spectra, and redox properties, Int. J. Quantum Chem. 116 (2016) 396–404.

[22] N. Vila, P.A. Aparicio, F. Secheresse, J.M. Poblet, X. López, I.M. Mbomekalle, Electrochemical behavior of alpha(1)/alpha(2)- $Fe(H_2O)P_2W_{17}O_{61}$ (7-) isomers in solution: experimental and DFT studies, Inorg. Chem. 51 (2012) 6129–6138.

[23] D. McGregor, B.P. Burton-Pye, I.M. Mbomekalle, P.A. Aparicio, S. Romo, X. López, J.M. Poblet, L.C. Francesconi, Tc-99 and Re incorporated into metal oxide polyoxometalates: oxidation state stability elucidated by electrochemistry and theory, Inorg. Chem. 51 (2012) 9017–9028.

[24] F. Doungmene, P.A. Aparicio, J. Ntienoue, C.S.A. Mezui, P. de Oliveira, X. López, I. M. Mbomekalle, Electrochemical behaviour of mixed d metal-iron containing Wells-Dawson sandwich-type complexes: $[(FeOH_2)_2M_2(X_2W_{15}O_{56})_2]^n$ and $[(MOH_2)_2Fe_2(X_2W_{15}O_{56})]_2^n$ (M = Cr-III, Mn-II, Mn-II, Co-II, Ni-II, Zn-II, X = As-V or P-V and n = 12 or 14), Electrochim. Acta 125 (2014) 674–682.

[25] J.M. Poblet, X. López, C. Bo, Ab initio and DFT modelling of complex materials: Towards the understanding of electronic and magnetic properties of polyoxometalates, Chem. Soc. Rev. 32 (2003) 297–308.

[26] X. López, J.J. Carbo, C. Bo, J.M. Poblet, Structure, properties and reactivity of polyoxometalates: A theoretical perspective, Chem. Soc. Rev. 41 (2012) 7537– 7571.

[27] X. López, P. Miró, J.J. Carbo, A. Rodriguez-Fortea, C. Bo, J.M. Poblet, Current trends in the computational modelling of polyoxometalates, Theor. Chem. Acc. 128 (2011) 393–404.

[28] X. López, C. Nieto-Draghi, C. Bo, J. Bonet Ávalos, J.M. Poblet, Polyoxometalates in solution: Molecular dynamics simulations on the a-$PW_{12}O_{40}^3$ Keggin anion in aqueous media, J. Phys. Chem. A 109 (2005) 1216–1222.

[29] F. Leroy, P. Miró, J.M. Poblet, C. Bo, J. Bonet Ávalos, Keggin polyoxoanions in aqueous solution: Ion pairing and its effect on dynamic properties by molecular dynamics simulations, J. Phys. Chem. B 112 (2008) 8591–8599.

[30] P. Miró, J.M. Poblet, J. Bonet Ávalos, C. Bo, Towards a computational treatment of polyoxometalates in solution using QM methods and explicit solvent molecules, Can. J. Chem. 87 (2009) 1296–1301.

[31] P.A. Aparicio, J.M. Poblet, X. López, Tungsten redox waves in $XMW_{11}O_{40}$ (n-) (X = P, Si, Al and M = W, Mo, V, Nb, Ti) Keggin compounds – Effect of localised/ delocalised charges, Eur. J. Inorg. Chem. (2013) 1910–1916.

[32] A. Klamt, G. Schüürmann, COSMO: A new approach to dielectric screening in solvents with explicit expressions for the screening energy and its gradient, J. Chem. Soc., Perkin Trans. 2 (1993) 799–805.

[33] L. Parent, P.A. Aparicio, P. de Oliveira, A.L. Teillout, J.M. Poblet, X. López, I.M. Mbomekalle, Effect of electron (de)localization and pairing in the electrochemistry of polyoxometalates: study of Wells-Dawson molybdotungstophosphate derivatives, Inorg. Chem. 53 (2014) 5941–5949.

[34] P.A. Aparicio, X. López, J.M. Poblet, Ability of DFT calculations to correctly describe redox potentials and electron (de)localization in polyoxometalates, Journal of Molecular and Engineering Materials 02 (2014) 1440004.

[35] L.C.W. Baker, J.S. Figgis, New fundamental type of inorganic complex: Hybrid between heteropoly and conventional coordination complexes. Possibilities for geometrical isomerisms in 11-, 12-, 17-, and 18-heteropoly derivatives, J. Am. Chem. Soc. 92 (1970) 3794–3797.

[36] M. Nyman, A.J. Celestian, J.B. Parise, G.P. Holland, T.M. Alam, Solid-state structural characterization of a rigid framework of lacunary heteropolyniobates, Inorg. Chem. 45 (2006) 1043–1052.

[37] J.P. Perdew, K. Burke, M. Ernzerhof, Generalized Gradient Approximation Made Simple, Physical Review Letters 77 (1996) 3865.

[38] A.J. Cohen, P. Mori-Sánchez, W. Yang, Challenges for Density Functional Theory, Chem. Rev. 112 (2012) 289–320.

[39] R. Ahlrichs, M. Bär, M. Häser, H. Horn, C. Kölmel, Electronic-structure calculations on workstation computers – The program system TURBOMOLE, Chem. Phys. Lett. 162 (1989) 165–169.

[40] O. Treutler, R. Ahlrichs, Efficient molecular numerical integration schemes, J. Chem. Phys. 102 (1995) 346–354.

[41] K. Eichkorn, F. Weigend, O. Treutler, R. Ahlrichs, Auxiliary basis sets for main row atoms and transition metals and their use to approximate Coulomb potentials, Theor. Chem. Acc. 97 (1997) 119–124.

[42] A.D. Becke, Density Functional thermochemistry. 3. The role of exact exchange, J. Chem. Phys. 98 (1993) 5648–5652.

[43] C.T. Lee, W.T. Yang, R.G. Parr, Development of the Colle-Salvetti correlation energy formula into a functional of the electron density, Phys. Rev. B 37 (1988) 785–789.

[44] C. Adamo, V. Barone, Toward reliable density functional methods without adjustable parameters: The PBE0 model, J. Chem. Phys. 110 (1999) 6158–6170.

[45] J.M. Tao, J.P. Perdew, V.N. Staroverov, G.E. Scuseria, Climbing the density functional ladder: Nonempirical meta-generalized gradient approximation designed for molecules and solids, Phys. Rev. Lett. 91 (2003).

[46] K. Eichkorn, O. Treutler, H. Öhm, M. Häser, R. Ahlrichs, Auxiliary basis sets to approximate Coulomb potentials, Chem. Phys. Lett. 242 (1995) 652–660.

[47] A. Schäfer, H. Horn, R. Ahlrichs, Fully optimized contracted Gaussian basis sets for atoms Li to Kr, J. Chem. Phys. 97 (1992) 2571–2577.

[48] M. Dolg, U. Wedig, H. Stoll, H. Preuß, Energy adjusted ab initio pseudopotentials for the 1st-row transition elements, J. Chem. Phys. 86 (1987) 866–872.

[49] D. Andrae, U. Häussermann, M. Dolg, H. Stoll, H. Preuß, Energy adjusted ab initio pseudopotentials for the 2nd and 3rd row transition elements, Theor. Chim. Acta 77 (1990) 123–141.

[50] L. Rulíšek, On the accuracy of calculated reduction potentials of selected group 8 (Fe, Ru, and Os) octahedral complexes, J. Phys. Chem. C 117 (2013) 16871– 16877.

[51] M.D. Tissandier, K.A. Cowen, W.Y. Feng, E. Gundlach, M.H. Cohen, A.D. Earhart, J.V. Coe, T.R. Tuttle, The proton's absolute aqueous enthalpy and Gibbs free energy of solvation from cluster-ion solvation data, J. Phys. Chem. A 102 (1998) 7787–7794.

[52] D.W. Smith, Ionic hydration enthalpies, J. Chem. Educ. 54 (1977) 540.

[53] A. Lewis, J.A. Bumpus, D.G. Truhlar, C.J. Cramer, Molecular Modeling of environmentally important processes: Reduction potentials, J. Chem. Educ. 81 (2004) 596–604.

[54] A. Bard, L. Faulkner, Electrochemical methods. Fundamentals and applications, 2nd ed., John Wiley & Sons, Inc., 2001.

[55] Y. Kato, Y. Shimizu, Y.J. Lin, K. Unoura, H. Utsumi, T. Ogata, Reversible half-wave potentials of reduction processes on nitroxide radicals, Electrochim. Acta 40 (1995) 2799–2802.

[56] M.C. Holthausen, Benchmarking approximate density functional theory. I. s/d excitation energies in 3d transition metal cations, J. Comp. Chem. 26 (2005) 1505–1518.

[57] C.J. Cramer, D.G. Truhlar, Density functional theory for transition metals and transition metal chemistry, Phys. Chem. Chem. Phys. 11 (2009) 10757–10816.

[58] K.P. Jensen, B.O. Roos, U. Ryde, Performance of density functionals for first row transition metal systems, J. Chem. Phys. 126 (2007) 014103-1-14.

[59] L.E. Roy, E. Jakubikova, M.G. Guthrie, E.R. Batista, Calculation of one-electron redox potentials revisited. Is it possible to calculate accurate potentials with Density Functional methods? J. Phys. Chem. A 113 (2009) 6745–6750.

[60] M. Srnec, J. Chalupsky, M. Fojta, L. Zendlova, L. Havran, M. Hocek, M. Kyvala, L. Rulíšek, Effect of spin-orbit coupling on reduction potentials of octahedral Ruthenium(II/III) and Osmium(II/III) complexes, J. Am. Chem. Soc. 130 (2008) 10947–10954.

[61] G. Fisicaro, L. Genovese, O. Andreussi, N. Marzari, S. Goedecker, A generalized Poisson and Poisson-Boltzmann solver for electrostatic environments, J. Chem. Phys 144 (2016) 014103.

[62] I. Borukhov, D. Andelman, H. Orland, Adsorption of large ions from an electrolyte solution: a modified Poisson-Boltzmann equation, Electrochim. Acta 46 (2000) 221–229.

[63] Y.H. Fang, G.F. Wei, Z.P. Liu, Theoretical modeling of electrode/electrolyte interface from first-principles periodic continuum solvation method, Catal. Today 202 (2013) 98–104.

[64] M. Garcia-Ratés, N. López, Multigrid-based methodology for implicit solvation models in periodic DFT, J. Chem. Theory Comput. 12 (2016) 1331–1341.